

A survey of pedestal magnetic fluctuations using gyrokinetics and a global reduced model for microtearing stability

Cite as: Phys. Plasmas **29**, 042503 (2022); <https://doi.org/10.1063/5.0084842>

Submitted: 10 January 2022 • Accepted: 26 March 2022 • Published Online: 12 April 2022

 M. T. Curie,  J. L. Larakers,  D. R. Hatch, et al.

COLLECTIONS

Note: This paper is part of the Special Collection: Papers from the 63rd Annual Meeting of the APS Division of Plasma Physics. Note: Paper UI1 2, Bull. Am. Phys. Soc. 66 (2021).

 This paper was selected as an Editor's Pick



[View Online](#)



[Export Citation](#)



[CrossMark](#)

Physics of Plasmas
Papers from 62nd Annual Meeting of the
APS Division of Plasma Physics

[Read now!](#)

A survey of pedestal magnetic fluctuations using gyrokinetics and a global reduced model for microtearing stability

EP

Cite as: Phys. Plasmas **29**, 042503 (2022); doi: 10.1063/5.0084842

Submitted: 10 January 2022 · Accepted: 26 March 2022 ·

Published Online: 12 April 2022



View Online



Export Citation



CrossMark

M. T. Curie,^{1,a)} J. L. Larakers,¹ D. R. Hatch,¹ A. O. Nelson,² A. Diallo,³ E. Hassan,^{4,5} W. Guttenfelder,³ M. Halfmoon,¹ M. Kotschenreuther,¹ R. D. Hazeltine,¹ S. M. Mahajan,¹ R. J. Groebner,⁶ J. Chen,⁷ DIII-D Team^{6,b)} C. Perez von Thun,⁸ L. Frassinetti,⁹ S. Saarelma,¹⁰ C. Giroud,¹⁰ JET Contributors^{c)} and M. M. Tennery¹

AFFILIATIONS

¹Institute for Fusion Studies, University of Texas at Austin, Austin, Texas 78705, USA

²Columbia University, New York, New York 10027, USA

³Princeton Plasma Physics Laboratory, Princeton, New Jersey 08536, USA

⁴Oak Ridge National Laboratory, Oak Ridge, Tennessee 37830, USA

⁵Physics, Faculty of Science, Ain Shams University, Cairo 11566, Egypt

⁶General Atomics, San Diego, California 85608, USA

⁷Department of Physics and Astronomy, University of California, Los Angeles, Los Angeles, California 90095, USA

⁸Institute of Plasma Physics and Laser Microfusion, Warsaw 01-497, Poland

⁹Division of Fusion Plasma Physics, KTH Royal Institute of Technology, Stockholm 114 28, Sweden

¹⁰CCFE, Culham Science Center, Abingdon OX14 3DB, United Kingdom

Note: This paper is part of the Special Collection: Papers from the 63rd Annual Meeting of the APS Division of Plasma Physics.

Note: Paper UI1 2, Bull. Am. Phys. Soc. **66** (2021).

^{a)}Invited speaker. **Author to whom correspondence should be addressed:** maxcurie@utexas.edu

^{b)}See the author list of Fenstermacher *et al.*, “DIII-D research advancing the physics basis for optimizing the tokamak approach to fusion energy,” Nucl. Fusion (2021).

^{c)}See the author list of Mailloux *et al.*, “Overview of JET results for optimising ITER operation,” in Nuclear Fusion Special issue: Overview and Summary Papers from the 28th Fusion Energy Conference, Nice, France, 10–15 May (2021).

ABSTRACT

This article presents a global reduced model for slab-like microtearing modes (MTMs) in the H-mode pedestal, which reproduces distinctive features of experimentally observed magnetic fluctuations, such as chirping and discrete frequency bands at noncontiguous mode numbers. Our model, importantly, includes the global variation of the diamagnetic frequencies, which is necessary to reproduce the experimental observations. The key insight underlying this model is that MTM instability is enabled by the alignment of a rational surface with the peak in the profile of the diamagnetic frequency. Conversely, MTMs are strongly stabilized for toroidal mode numbers for which these quantities are misaligned. This property explains the discrete fluctuation bands in several DIII-D and JET discharges, which we survey using our reduced model in conjunction with global gyrokinetic simulations. A fast yet accurate reduced model for MTMs enables rapid interpretation of magnetic fluctuation data from a wide range of experimental conditions to help assess the role of MTM in the pedestal.

Published under an exclusive license by AIP Publishing. <https://doi.org/10.1063/5.0084842>

I. INTRODUCTION

Tokamak confinement has greatly improved with the advent of the H-mode,¹ an operational regime with a plasma edge region characterized by sharp density and temperature gradients known as the pedestal. The H-mode pedestal boosts the plasma pressure in a narrow region at the edge of the plasma. Due to this high edge pressure, the core plasma, which is typically limited by stiff ion-scale transport, will be able to attain the high pressures necessary for burning plasmas. While the pedestal results from the strong reduction of transport in the edge (i.e., a transport barrier),² there remain microinstabilities that limit pedestal gradients and account for most of the edge transport. As a consequence of the importance of the pedestal to plasma confinement, it is critical to identify and understand the remaining pedestal transport mechanisms. This is crucial, for example, to understand and predict naturally edge-localized modes (ELM)-free scenarios and the properties of pedestals in unfamiliar parameter regimes like those envisioned for burning plasmas.

Several recent studies^{3–9} have shown that microtearing modes (MTMs) are responsible for prominent magnetic fluctuations observed in the pedestal.^{10–21} Edge modeling predicts that the electron heat diffusivity far surpasses the particle diffusivity:²² $D/\chi \ll 1$. This means that a substantial electron heat transport mechanism must be active. electron temperature gradient (ETG) and MTM are the most likely candidates, and gyrokinetic simulations suggest that they are both active in the pedestal depending on parameters. Nonlinear gyrokinetic simulations have demonstrated that MTM transport is comparable to experimental expectations in several recent studies.^{3,5,6} Reference 3 also presents an inter-ELM profile analysis showing that the electron temperature gradient saturates, at the same time, as the quasi-coherent fluctuations (QCFs), which are shown to be MTMs. The density gradient and the ion temperature and impurity density are un-correlated with the QCF. Experimentally, Ref. 4 identifies MTMs as the source of observed magnetic fluctuations and finds that their activity is correlated with a reduction in confinement.

Gyrokinetic simulations have been performed to provide more evidence for the presence of pedestal MTMs and have given a guideline for future experiments. However, simulations suffer from high sensitivity to initial conditions and experimental data have a degree of uncertainty. Also, accurate gyrokinetic simulations of the pedestal are computationally intensive. Consequently, more-efficient models are highly desirable.

This paper focuses on the identification of MTM in magnetic signals commonly observed in the pedestal. Recent work^{6,7,23,24} has shown that global gyrokinetics (but not local) can reproduce distinctive band structures in a magnetic spectrogram. The band structures can be understood from the fundamental properties of microtearing modes. Global gyrokinetics encompasses all the physics necessary to reproduce these modes. However, simulation results are exceedingly sensitive to the details of the equilibrium reconstruction. Proper validation requires extensive statistical sampling of background profiles and equilibria within error bars, which can be computationally demanding with global gyrokinetic simulations, especially when applied to an extensive set of discharges. The goal of this work is to formulate and test reduced models that can capture these physics in order to (1) validate the theory more extensively and (2) provide a tool for the broader community for rapid analysis of magnetic fluctuation

data. These tools may ultimately inform equilibrium reconstruction by providing a constraint on the range of safety factor within the pedestal.

This article introduces an unstable MTM identification scheme, which is intended to predict thresholds and fluctuations bands (toroidal mode numbers and frequency bands) without resorting to gyrokinetic simulations. The model is simple and fast enough to be able to apply to a broad experimental database, independent of the device. We call this method the slab-like microtearing mode (SLiM) model. A set of global gyrokinetic simulations using GENE^{25,26} will be compared with the results from the SLiM model. The sensitivity of stability of the MTM due to the change of safety factor profile has been studied by GENE simulations and SLiM dispersion calculations.

The article has the following structure: Sec. II A, the theoretical foundation will be described: a reduced global analytical model of the microtearing mode.²³ In Secs. II A, B, and C, the method of finding unstable MTM's will be introduced. Section III will offer a list of discharges studied by such a method. In Sec. IV, we will discuss the study of the discharges and possible ways to use the result in equilibrium fitting.

II. THE SLAB-LIKE MTM (SLiM) MODEL FOR IDENTIFYING MTM FLUCTUATIONS

Recent work by Hassan⁷ displays evidence that there are two types of MTM in the pedestal. The lower-frequency MTM is well described by a slab model,²³ which does not include information about toroidal geometry. In contrast, the higher-frequency collisionless MTM is sensitive to details of the magnetic geometry. The work of this paper focuses on the slab-like MTM only. The study of the collisionless MTM is an active area of research and beyond the scope of this paper.

In this paper, we apply three models to simulating and predicting slab MTM instability, as outlined in Table I. It goes from complex to simple from the top to the bottom of the chart. The global linear gyrokinetic simulations using GENE²⁵ represent a first-principles approach to this problem. Such simulations consume about 10 000 core hours per mode (entailing a scan in toroidal mode number) while providing comprehensive information of the given mode. We also apply the slab-like MTM (SLiM) model for identifying MTM fluctuations. This model includes two modes of operation: (1) a solver for a global MTM dispersion relation which will be referred to as SLiM (dispersion) and (2) a fast mode of operation applying simple heuristics to identify toroidal mode numbers that may have unstable MTM. This mode of operation will be referred to as SLiM (alignment). These models are described in detail in Secs. II A, B, and C.

In Subsection II A, we begin with a brief survey of the background theory. Following this, we describe the slab-like MTM (SLiM) model for identifying MTM fluctuations in detail.

A. Theoretical background

Figure 1 shows the pressure profile in a typical H-mode discharge. The green shaded region denotes the pedestal where the pressure exhibits a dramatic rise going from the edge toward the core plasmas. The red line marks the mid-pedestal (top plot) which is also the location of the peak of the pressure gradient and electron diamagnetic frequency

$$\omega_{*e} = k_y \rho_s c_s \left(\frac{1}{L_{n_e}} + \frac{1}{L_{T_e}} \right),$$

TABLE I. The models used in this paper (ranked by the most computationally expensive to the cheapest): global linear gyrokinetic simulations, SLiM (dispersion calculation), SLiM (alignment of rational surfaces and ω_{*e} peak).

Model	Physics	Output	Time consumed (s)
Global linear simulation	Gyrokinetic	Moments of species	10^7
SLiM (dispersion)	Global slab model dispersion	Growth rate, frequency	10^2
SLiM (alignment)	Alignment of rational surfaces to peak	Unstable/stable	1

where $k_y = \frac{n_{tot}q}{L}$, $a/L_{n_e} = \frac{1}{n_e} \frac{dn_e}{d\rho_{tor}}$, $a/L_{T_e} = \frac{1}{T_e} \frac{dT_e}{d\rho_{tor}}$, $c_s = \sqrt{\frac{T_e}{m_i}}$, $\rho_s = \frac{mc_s}{eB}$ (a is the minor radius). We also direct the reader to Appendix B in Ref. 6 for several expressions for ω_{*e} in terms of different radial coordinates.

The microtearing mode (MTM) is driven by electron temperature gradients $\frac{a}{L_{T_e}}$. The original slab mode,²⁷ which is of interest here, also requires the collision frequency to be comparable to ω_{*e} (other branches of MTM can be unstable at low collisionality in the pedestal⁷). Beyond these dominant parameter dependencies, the mode is also sensitive to $\eta = \frac{L_n}{L_T}$, \hat{s} (magnetic shear), $\beta = \frac{P_{\text{thermal}}}{P_{\text{magnet}}}$, and $k_{||}$.^{27,28} However, a recent discovery⁶ showed that MTM stability in the pedestal is also sensitively dependent on the alignment of rational surfaces with the peak in ω_{*e} . This discovery provides an elegant explanation for the discrete frequency bands at disparate toroidal mode numbers that are often observed in magnetic fluctuation data. A simplified model²³ that captures this effect is described in Subsection II B.

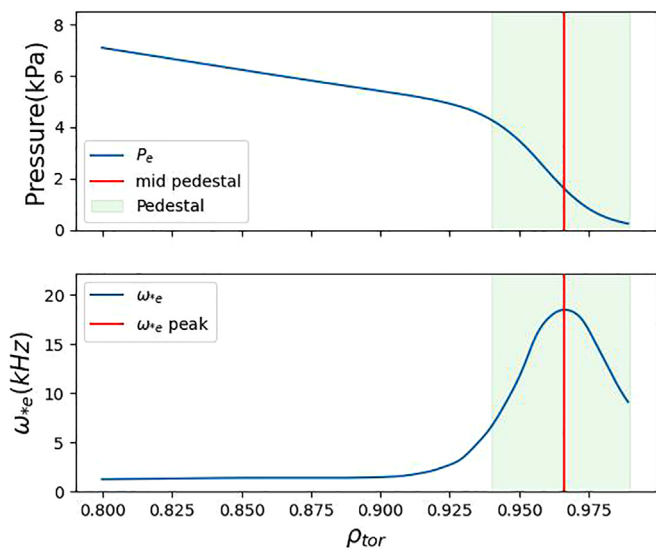


FIG. 1. The plot shows the common H-mode pedestal: the pressure (top) and ω_{*e} (bottom). The red line marks the mid-peDESTAL. Green shade is considered pedestal.

B. The slab-like MTM (SLiM) model for identifying MTM fluctuations-global dispersion solver

This phenomenon of “offset stabilization,” wherein MTMs are stabilized due to misalignment between a rational surface and the peak of the ω_{*e} profile, was clearly elucidated using a global reduced model of MTM stability by Larakers *et al.*,²³ which is a key component of the SLiM model. In the current paper, the term global is used to denote that a model retains variation of background quantities and solves for a radial eigenmode, in contrast with the local flux tube approach. This work determined that a global treatment of the problem was necessary to capture the effect of the rational surface alignment and identified the key parameters governing this phenomenon.

The reduced model solves the dispersion relation defined by the following equations:

$$\frac{d^2 A_{||}}{dx^2} = -\frac{4\pi}{c} \sigma_{||}(\omega, x) E_{||}, \quad (1)$$

$$\left(\frac{c}{v_A}\right)^2 (\omega - \omega_{*e}) \frac{d^2 \phi}{dx^2} = -4\pi k_{||} \sigma_{||}(\omega, x) E_{||}. \quad (2)$$

Here, $A_{||}$ is the magnetic vector potential that is parallel to the magnetic field B_0 , ϕ is the electric potential, $E_{||}$ is the electric field that parallels to B_0 , $\sigma_{||}(\omega, x)$ is the conductivity²⁴ parallel to B_0 (calculated based on full-Landau collision operator, see the Appendix for more detail), c is the speed of light, x is the distance from the rational surface to the ω_{*e} peak normalized to gyroradius, v_A is the Alfvén velocity, $k_{||} = \hat{b} \cdot \mathbf{k}$, and Eq. (2) is calculated from quasi-neutrality using kinetic theory. Equation (1) is derived using Ampère’s law and Ohm’s law.

Those two equations can be used to solve the dispersion relation for the slab MTM $\omega(k_y, \eta, \hat{s}, \beta, \nu, \mu, x_*)$. A major result from the model is elucidation of offset stabilization—the reliance of MTM stability on the alignment of the rational surfaces with the peak of ω_{*e} which can be parameterized by μ/x_* . The quantities μ and x_* are illustrated in Fig. 2. μ is defined as the distance from the rational surface to the ω_{*e} peak, and x_* is the spread of ω_{*e} as estimated from a Gaussian fit. Both μ and x_* are normalized to sound gyroradius $\rho_s = c_s/\omega_{*e}$. $\frac{\mu}{x_*}$ provides a relative distance of the rational surfaces to the ω_{*e} peak. The formal definition can be found in the Larakers’ paper.²³ In addition, further discussion of MTM stability dependence on μ/x_* can be found at the end of Sec. IV in the context of global gyrokinetics simulations.

Figure 3 shows an example of the dependence of the MTM growth rate as the rational surfaces go away from the ω_{*e} peak calculated from SLiM dispersion relation. In this case, the growth rate drops over 85% as μ/x_* goes from 0 to 0.3. This criterion— $\mu/x_* < 0.3$, $\mu_{crit} \equiv 0.3x_*$ —corresponds to the top 8% of the ω_{*e} shown in the purple highlighted area Fig. 4, roughly denoting the radial region within which a rational surface must lie in order for an MTM to be unstable.

We can derive a simple criterion for the critical toroidal mode number below which the phenomenon of offset stabilization may occur. The difference of safety factor between two rational surfaces for toroidal mode number n is $\delta q = 1/n$, and then the distance between rational surfaces can be calculated as $\delta\rho_{tor} = \delta q / \left(\frac{dq}{d\rho_{tor}} \right)$. Plug in the

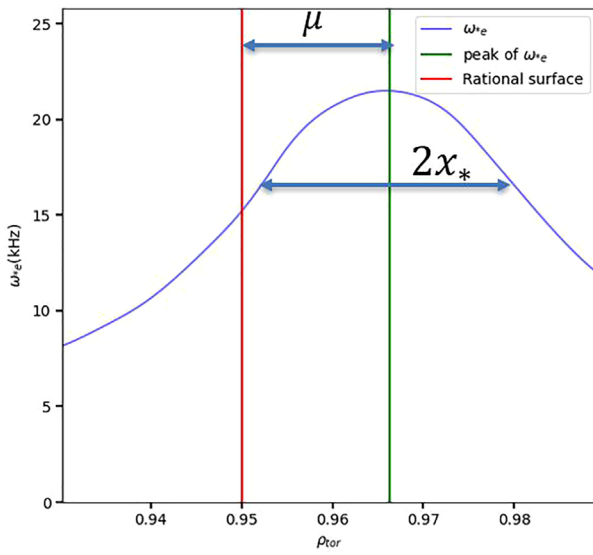


FIG. 2. The definition of the μ and x_* . μ is the distance from the rational surface (red) to the peak of ω_{*e} (green). x_* is the spread of the ω_{*e} which is proportional to σ in Gaussian function.

definition of the magnetic shear $\hat{s} \equiv \frac{\rho_{\text{tor}}}{q} \frac{dq}{d\rho_{\text{tor}}}$. The distance between rational surfaces is

$$\delta\rho_{\text{tor}} = \frac{\rho_{\text{tor}}}{nq\hat{s}}. \quad (3)$$

For n greater than n_{crit} , there will be more than one rational surface within the range of $\delta\rho_{\text{tor}} = \frac{\rho_{\text{tor}}}{nq\hat{s}}$ and the radial stability boundary $\mu_{\text{crit}} = \delta\rho_{\text{tor}}/2$, and then the rational surfaces will not be subjected to

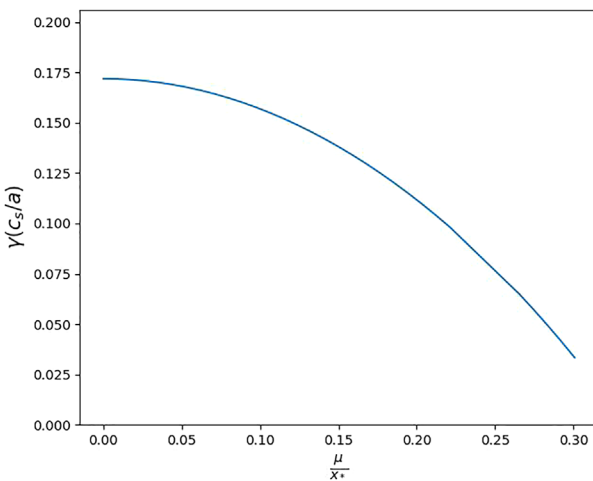


FIG. 3. MTM growth rate dependence on μ/x_* for toroidal mode number $n = 3$ with parameters taken from DIII-D discharge 174819 (further description can be found in the Sec. IV).

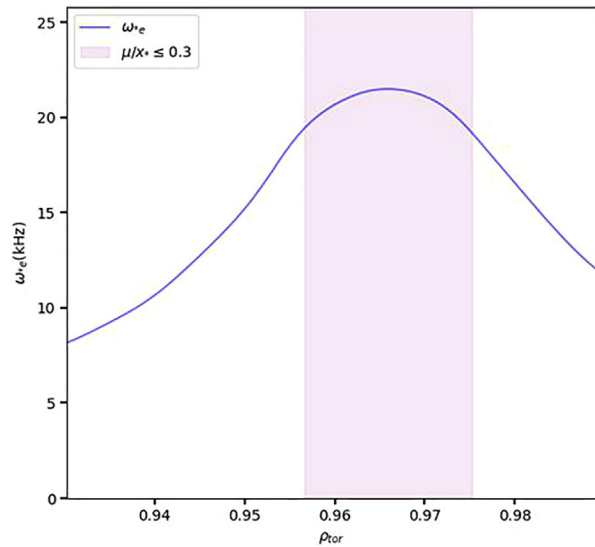


FIG. 4. Profile of ω_{*e} along with a shaded region denoting the top 8% of the ω_{*e} . Rational surfaces in this shaded region can potentially host unstable MTM for $n = 3$.

offset stabilization effect. One can calculate the n_{crit} by plugging $\delta\rho_{\text{tor}} = 2\mu_{\text{crit}}$ into Eq. (3)

$$n_{\text{crit}} = \frac{\rho_{\text{tor}}}{2\hat{s}q\mu_{\text{crit}}}. \quad (4)$$

C. The slab-like MTM (SLiM) model—alignment mode

Figure 5 presents a faster way to determine the toroidal mode numbers at which MTMs are potentially unstable based on the theory presented in Sec. III B. As discussed above, MTMs are most prone to instability near the peak of the electron diamagnetic frequency ω_{*e} , providing a radial stability boundary (two orange vertical lines). The frequency constraints (two purple horizontal lines) can be calculated from an analytical model (likely even a local model) or observed from experimental frequencies extracted from magnetic fluctuation data. The four lines create a highlighted area (blue rectangle) where the MTM is likely to become unstable. Since the MTMs are localized around rational surfaces, if the intersection (blue dot) of the rational surfaces (red line) and the ω_{*e} falls inside of the highlighted rectangle, then the toroidal mode number corresponding to that rational surface may host an unstable MTM. One ambiguity, which we will discuss in more detail below, is that the MTM appears to relax the electron temperature gradient in the vicinity of the rational surface in some scenarios, thus also decreasing the local ω_{*e} below a standard (e.g., tanh) profile fit.^{3,6}

To further illustrate the model, we will provide another hypothetical case with a stable rational surface in Fig. 6 (scenarios from actual experimental discharges will be shown below). Here, the rational surface (red vertical line) intersects with ω_{*e} curve outside of the unstable area, suggesting that there will be no unstable MTM at this rational surface.

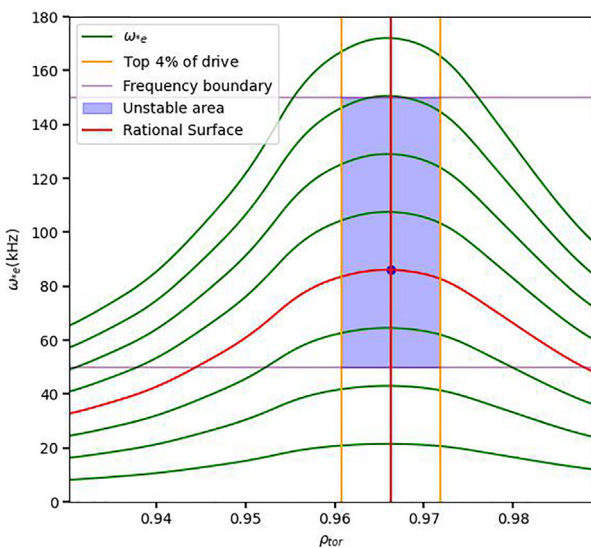


FIG. 5. Possible region for unstable MTM: The green curves are the plot of $\omega_{e,tot}^*$ with different toroidal mode numbers with $n = 1$ at the bottom and increase while going up, red marks the unstable ones. The blue shaded area is the unstable region considering the top 4% drive (two orange vertical lines) and frequency boundary 50 to 150 kHz (two purple horizontal lines). The blue dot is the intersection between the $\omega_{e,tot}^*$ curve and the corresponding rational surface (red vertical line). If the dot falls into the blue region, then it is unstable.

III. APPLICATIONS TO DISCHARGES

In this section, we apply gyrokinetic simulations and the SLiM model to a set of discharges in order to (1) demonstrate the validity of

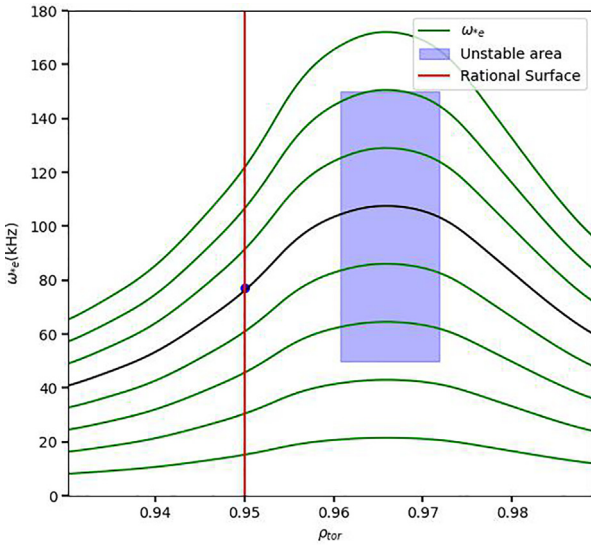


FIG. 6. The plot shows $\omega_{e,tot}^*$ with different toroidal mode numbers (green and black curves) with $n = 1$ at the bottom and increases while going up. And the rational surface (red vertical line) intersect with $\omega_{e,tot}$ curve (black curve) at the blue dot outside of the unstable area (blue rectangle, defined at Fig. 5). This suggests that $n = 1$ will not produce an unstable MTM.

the physical picture outlined above and (2) discuss the potential applications of the model such as

- Predicting the toroidal mode numbers of unstable MTMs.
- Determining poloidal mode numbers corresponding to experimentally observed magnetic fluctuations.
- Constraining the safety factor in the pedestal region for equilibrium reconstruction.

We will survey four discharges: three from DIII-D (162940, 174864, and 174819) and one from JET (78697). Various aspects of three of these discharges are discussed in separate publications,^{6–8} while the analysis of DIII-D shot 174819 is entirely original to this paper. Collectively, these analyses demonstrate the power of the theoretical concepts outlined above for predicting and interpreting magnetic fluctuation data and outline some useful applications of the SLiM model.

A. DIII-D discharge 162940

We first review an analysis of DIII-D discharge 162940 described in Ref. 7. Figure 7 shows the magnetic spectrogram from Mirnov coils at two time scale. The frequency bands of interest, which are highlighted with the white outline in the middle plot, are those that are correlated with the inter-ELM cycle increasing with $\omega_{e,tot}$ as the pedestal gradients recover. Note that the thin, bright bands are not (or weakly) correlated with the ELM-cycle and correspond to core modes, which are not of interest here. The global linear gyrokinetic simulations find unstable MTMs at toroidal mode numbers and frequencies in good agreement with the fluctuation data. Notably, the lowest toroidal mode number with an unstable MTM is at $n = 3$ with a frequency 65 kHz. The corresponding frequency band in the spectrogram can be identified as $n = 3$ in agreement with this result (after factoring in a possible nonlinear frequency downshift). The global GENE simulations find additional low- n MTMs at $n = 5, 6$ in agreement with the other highlighted band 85–110 kHz. The higher toroidal mode number MTMs $n = 17–28$ correspond closely with a high-frequency band 290–500 kHz in the left-most plot. These modes are identified as curvature-driven MTM in Ref. 7. In short, global GENE simulations are capable of reproducing a very distinctive band structure almost quantitatively with precise agreement on the toroidal mode number of the lowest frequency band (i.e., the only band for which a toroidal mode number can be identified). The linear frequencies are at the high range of the frequency bands. This is likely due to the nonlinear relaxation of the temperature gradient around rational surfaces, which was discussed in detail in Ref. 6. In that reference, it was shown that the temperature gradient relaxes around the rational surface, which, in turn, decreases the diamagnetic frequency $\omega_{e,tot}$.

The discussion thus far in the present subsection is a review of the results described in Ref. 7. Subsection III A 1 will describe the new application of the SLiM model to this discharge.

1. Application of SLiM to DIII-D discharge 162940

The SLiM is limited to the slab MTM active at low toroidal mode numbers (i.e., it is not applicable to the curvature-driven MTMs at $n = 17–28$ described above). Here, we test its effectiveness for this discharge. The SLiM model will be applied for the toroidal mode number less than 15. Figure 8 shows the rational surfaces (n, m) = (5, 23),

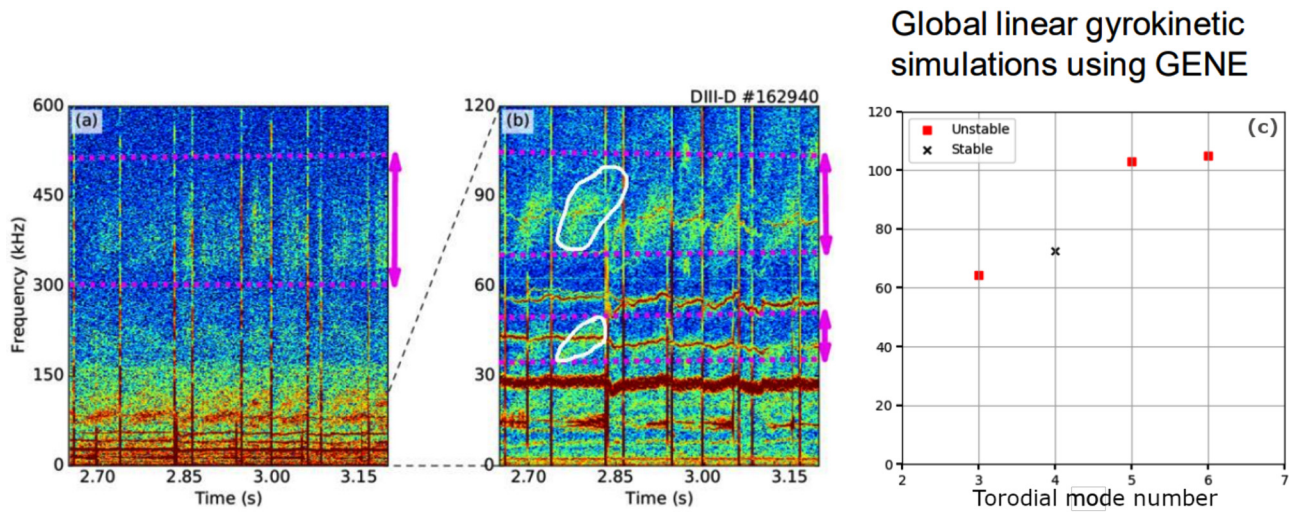


FIG. 7. DIII-D discharge,⁷ left plot and middle plot (a) and (b): magnetic spectrogram observed from Mirnov coils, left plot(a): shows the frequency from 0 to 600 kHz, one can see the broad magnetic frequency band from 290 to 500 kHz; the middle plot(b) zooms in frequency to 0 to 120 kHz, the white circles highlight the two frequency bands 45–55, 85–110 kHz; the right plot(c) shows the global linear simulations from $n = 3$ to $n = 6$, red dots are the simulations with unstable MTM, the gray cross (x) is the stable mode.

(3, 14), and (6, 28) [which align with the ω_{*e} peak, where (3, 14) and (6, 28) are in the same radial location] along with the ω_{*e} profiles corresponding to the relevant toroidal mode numbers. As seen in the figure, the SLiM (alignment) model effectively predicts the three unstable mode numbers identified in the global linear gyrokinetic simulations.

Figure 9 shows the growth rates and frequency calculated from the SLiM dispersion solver and global linear GENE simulations. While there are quantitative differences, both models successfully predict the

unstable toroidal mode numbers and frequencies identified in the magnetic spectrogram. This suggests that SLiM may be a fast and effective approach to predicting and interpreting magnetic fluctuations.

The SLiM model successfully predicts the mode number $n = 3, 5, 6$ to be unstable. Since the SLiM model is limited to slab-like MTM, it is not applicable to the MTM at toroidal mode number higher than 15. For the high toroidal mode number, the local linear simulations predicted the broad frequency band of unstable MTM. The local linear simulations provide similar results as the global linear calculations at $n_\phi \geq 15$ in Fig. 3 and Fig. 6 in publication by Hassan.⁷ It is worth noting that the local simulations failed to explain the gap of the low-frequency bands from 55 to 85 kHz. In other words, the local linear

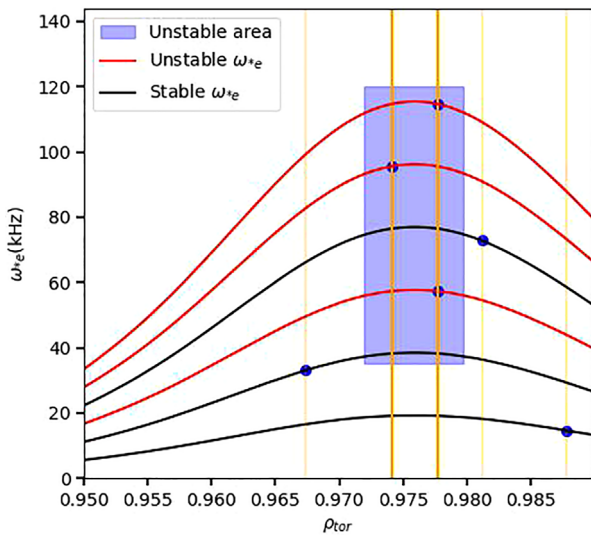


FIG. 8. Unstable MTM predicted by the SLiM model using rational surface alignment: blue highlighted region is the unstable area with location and frequency constraint discussed in Sec. III. Orange vertical lines are the rational surfaces. The blue dots are the intersection of between the rational surfaces with the ω_{r*} curves. The red curves are ω_{r*} for the toroidal mode numbers that are unstable, and black are stable.

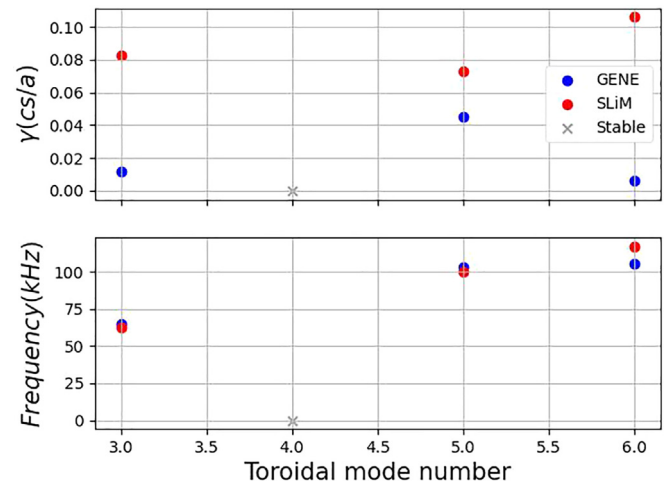


FIG. 9. Growth rate (top) and frequency in the lab frame (bottom) calculated from SLiM (red) and global linear GENE simulations (blue). The stable mode is marked with black cross. The left y axis is for GENE, and the right y axis is for SLiM.

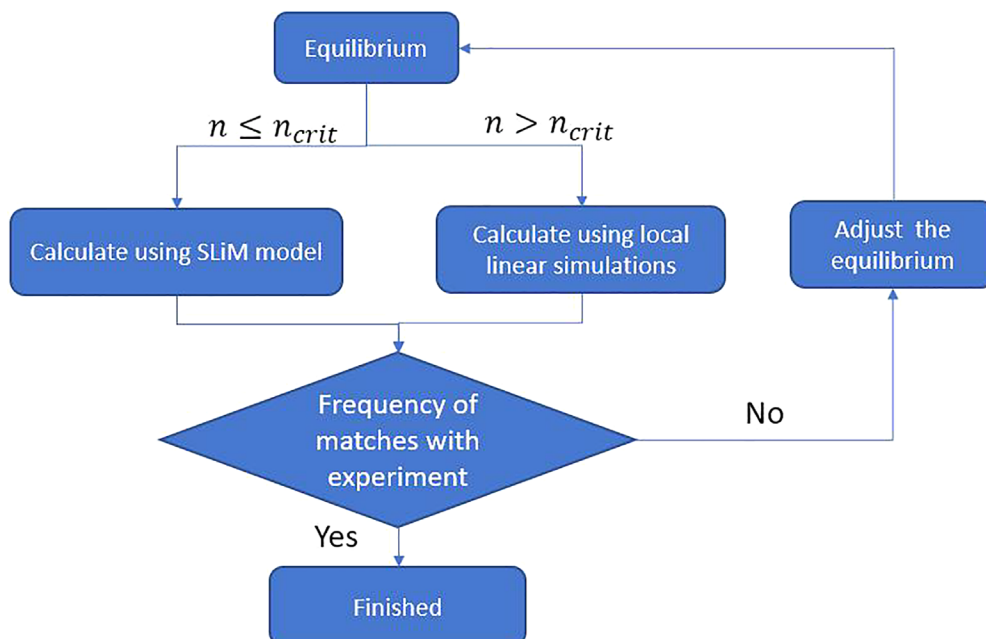


FIG. 10. The flow chart on determining the unstable MTM using SLiM and local linear gyrokinetic simulations.

simulations failed to predict $n=4$ being stable. This mode skipping phenomenon is caused by the lack of alignment of the rational surfaces with the ω_{ce} peak, which is a global effect.

Figure 10 shows the suggested workflow on matching the potential MTM using the SLiM model and local linear simulations. For the toroidal mode number less than 15, the MTM is likely to be slab-like which can be calculated from SLiM. Since the rational surfaces are not densely packed for low-mode number cases [$n \leq n_{crit}$, recall n_{crit} from Eq. (4)], a global effect is needed in order to find the corresponding discrete frequency bands, which SLiM is capable of doing. For the mode number greater than n_{crit} the rational surfaces are so densely packed that the discrete band will not be observed, plus that MTM with high mode numbers requires more physics than a slab-like approximation to determine. Therefore, the local linear simulations will be a good complement to the SLiM model for matching all the magnetic frequency bands in the experiment that are likely to be MTM. Since local gyrokinetic simulations are relatively cheap computationally, this can be done routinely and extensively.

With experience from these cases, we come up with a recipe for the future calculation of the potential unstable MTM that is far less computationally intensive than the current routine: use the SLiM model to find the unstable MTM at $n_\phi < n_{crit}$ and then use the local linear calculation to find the unstable MTM at $n_\phi \geq n_{crit}$. Such a method could greatly reduce analysis time with respect to a global gyrokinetic analysis.

B. JET discharge 78697

We now turn to JET discharge 78697. The connections between MTMs and the magnetic fluctuations in this discharge are described in Ref. 6. Figure 11 shows that global linear GENE simulations reproduce the fluctuations at $n=4$ and $n=8$ (red dash lines) observed in the

magnetic spectrogram with light blue ($n=4$) and blue ($n=8$) bands. These results required a slight modification of the q profile to ensure alignment of the relevant rational surfaces. The linear simulations produce frequencies that are somewhat higher than those in the fluctuation bands. However, global nonlinear simulations exhibit electron temperature profiles that locally flatten in the region surrounding the rational surface, producing downshifted and broadened frequency bands matching the results of the experiment.²³

This discharge was studied with the SLiM dispersion solver,²³ which we briefly review here along with global gyrokinetic simulations.

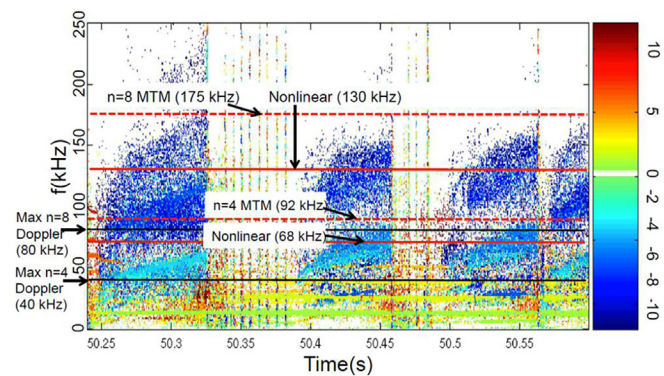


FIG. 11. JET discharge 78697, where red solid lines are the frequency calculated from global nonlinear simulations, the solid black lines are global nonlinear calculated frequency after adding the maximum Doppler shift within experimental uncertainty, and the red dash lines are the frequency calculated from global linear simulations. Reproduced with permission from Hatch *et al.*, Nucl. Fusion **61**, 036015 (2021).⁶ Copyright 2021, IOP Publishing.

Figure 12 shows the relevant rational surfaces. Note that mode numbers $(n, m) = (4, 11), (8, 22), (12, 33)$ (red vertical line) align with the peak of ω_{*e} (blue curve), while other rational surfaces lie much farther away.

Figure 13 shows the comparison between the SLiM dispersion solver and global linear GENE simulations. While there are quantitative differences, both models predict unstable MTMs at $(n, m) = (4, 11), (8, 22), (12, 33)$ (GENE also predicts a very weakly unstable MTM at $n=9$). Note that the $n=12$ mode is not observed in the spectrogram. Several plausible explanations are discussed in Ref. 6. This scenario provides additional evidence of the interpretive power of the SLiM model.

C. DIII-D discharge 174864

Analysis of DIII-D discharge 174864 is described in detail in Ref. 8, which traces the frequency of a magnetic fluctuation band throughout the inter-ELM period and predicts the poloidal mode number of the fluctuation based on the concepts of the rational surface alignment described above.

In this discharge, the toroidal mode number is identified experimentally to be smaller than $n = 10$ with relative certainty using code MODESPEC.²⁹ However, the poloidal mode number cannot be directly extracted from the experimental data. By using the idea of the rational surface alignment along with the corresponding frequency of ω_{*e} at the given rational surface, one can trace the frequency band that is likely to be MTM and determine the poloidal mode number by matching the shape of the frequency band predicted by such concepts with experimental observation. As Fig. 14 shows the frequency can be calculated by plotting all rational surfaces with different poloidal numbers (left plot) and calculating the frequency at each time slice will provide frequency bands with different poloidal mode numbers (middle plot). By overlaying the frequency bands predicted by the model with the magnetic spectrogram (right plot), one can find that the poloidal mode number $m = 16$ matches the experiment. Therefore, the poloidal mode number for that given frequency is likely to have a poloidal mode number of $m = 16$.

Figure 15 provides a workflow for identifying poloidal mode numbers. One can find the toroidal mode number from the experimental fluctuation data.²⁹ With profile fits and an equilibrium calculated from

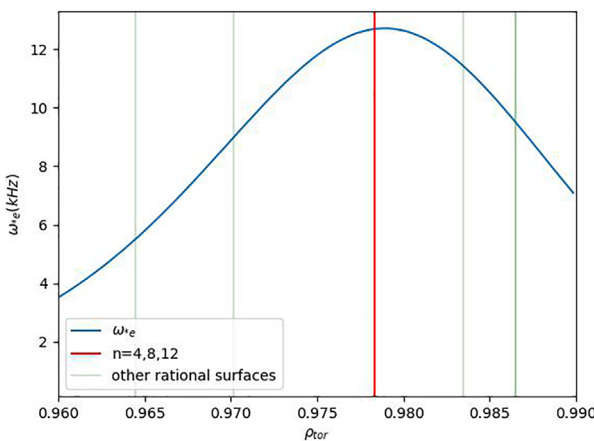


FIG. 12. The plot shows the rational surfaces $n = 4, 8, 12$ (red vertical line) aligned with the ω_{*e} , while other rational surfaces (green) are further way.

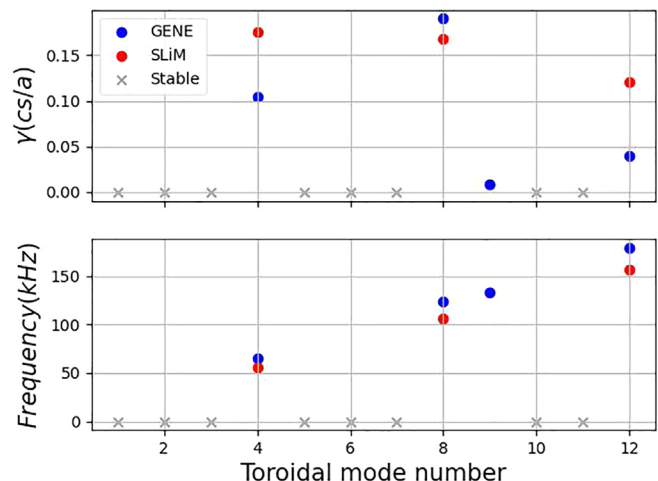


FIG. 13. This plot shows the comparison of the growth rate (top) and frequency in the lab frame (bottom) between SLiM dispersion relation calculations (red) and global linear GENE simulations (blue).²³ The gray crosses are the stable modes.

kinetic equilibrium fitting (EFIT),³⁰ one can find the corresponded frequency with different poloidal mode numbers. If the shape (chirping) of the frequency can be matched with the magnetic spectrogram in the experiment, then that frequency band is likely to have that poloidal mode number.

D. DIII-D discharge 174819

Finally, we analyze DIII-D discharge 174819, once again demonstrating the capacity of SLiM to reproduce and interpret the fluctuation data while also outlining potential applications for refining equilibrium reconstructions.

Clearly, the placement of the rational surfaces of low mode numbers is highly sensitive to the q profile. For equilibria with low magnetic shear, this can result in extreme sensitivity of unstable MTMs to the q profile. Figure 16 shows that the rational surfaces' location will change from the stabilizing location (red vertical line) off the peak of ω_{*e} to the destabilizing position (green vertical line) at the peak by reduction of the q profile by 2%. Such sensitivity can be exploited for the q profile constraint at the pedestal region for a potentially more accurate equilibrium fitting.

Such sensitivity has been a challenge for simulating MTMs using global gyrokinetics.^{3,6} Sometimes, extensive sensitivity tests are needed to match the observed fluctuation bands. The SLiM model provides a unique perspective on the sensitivity to the safety factor. The DIII-D discharge 174819 is a good case for showcasing the capabilities of the SLiM model. As Fig. 17 shows, there are two magnetic frequency bands that are likely to be MTM, with toroidal mode number of $n = 3$ with a frequency of 63 kHz, while the higher band has $n = 5$ with a frequency of 110 kHz. The toroidal mode numbers are determined by the code MODESPEC²⁹ using only the experimental data. The expected frequency of the MTM is ω_{*e} for the radial location of the eigenmode.

Figure 18 plots the ω_{*e} for $n = 1$ and safety factor. The orange vertical lines roughly denote the radial stability boundary (top 8% of ω_{*e}). Since the frequency of peak ω_{*e} (including the Doppler shift) is about 22 kHz for $n = 1$ from Fig. 18, then the frequency of ω_{*e} peak

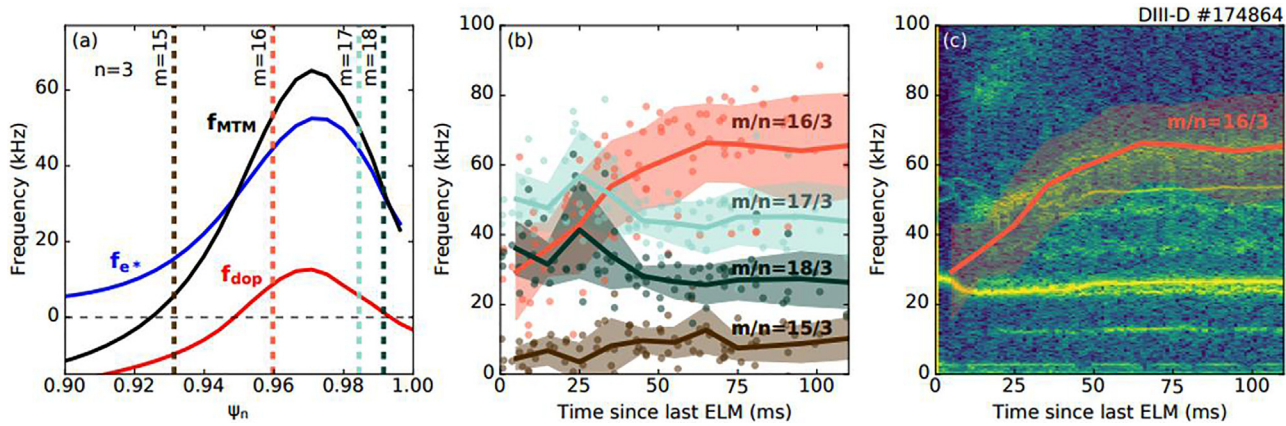


FIG. 14. Left plot (a) shows the alignment of the rational surfaces and the ω_{*e} . Middle plot (b) shows the frequency bands with different poloidal mode numbers predicted, the right plot (c) shows the overlay of the frequency band that matches the best with experimental observation. Reproduced with permission from Nelson *et al.*, Nucl. Fusion 61, 116038 (2021).⁸ Copyright 2021, IOP Publishing.

for $n = 3$ and $n = 5$ is 66 and 110 kHz, respectively. Therefore, comparing with experimentally observed frequency of 63 kHz for $n = 3$, and 110 kHz from $n = 5$, we can determine that $n = 3$ and $n = 5$ are likely to be unstable MTM. As shown below, we can also explain and reproduce the absence of the $n = 4$ and $n = 6$ fluctuations.

In order to match the experimental observation ($n = 3, 5$), we can change the q profile so that the desired toroidal mode numbers will host unstable MTM while keeping the rest stable. As Fig. 19 shows, the values of q with toroidal mode numbers 3 (red), 4 (green), and 5 (orange) are the horizontal lines bounded by the radial stability boundary. The rational surface will have an unstable MTM if the q profile curve goes through the horizontal line corresponding to that

toroidal mode number. The radial location at which the horizontal lines intersect with the q profile is the location where the MTM will be localized. The closer the intersection is to the center dot of the horizontal line, the more unstable the MTM will be. The procedure, then, is to modify the q profile (within reasonable uncertainties) so that the safety factor curve goes through the horizontal lines corresponding to the desired (experimentally observed) toroidal mode numbers while avoiding the stable ones. For this discharge, we will need to modify the q profile so that it goes through $n = 3$ (orange) and $n = 5$ (red) while avoiding $n = 4$ (green). The nominal profile goes through toroidal mode numbers 4 (green) and 5 (red) while avoiding 3 (orange). By downshifting by 2%, these criteria are satisfied.

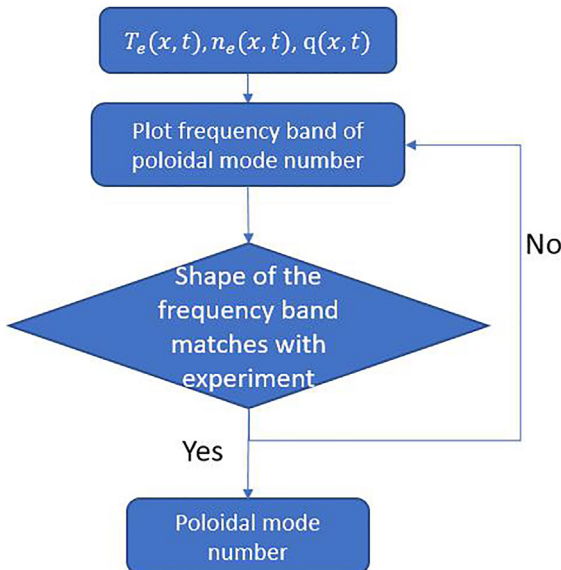


FIG. 15. The flow chart for finding the poloidal mode number: one can take the equilibrium and calculate the frequency band with different poloidal mode numbers and check if the frequency matches with the experimental observation.

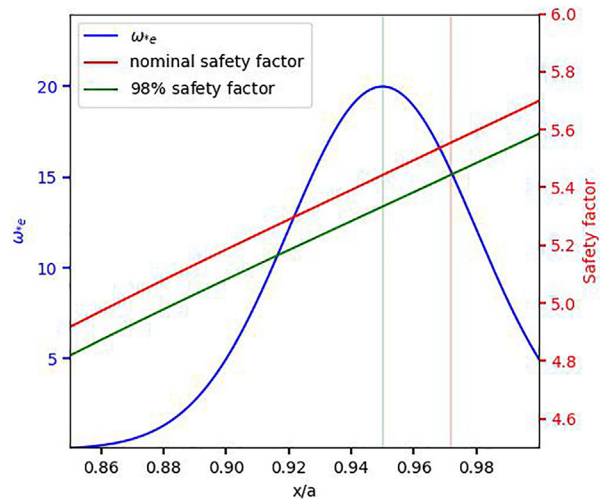


FIG. 16. Demonstration of the sensitivity of the rational surfaces to variations of the q profile. The blue curve is the ω_{*e} profile (left y axis), and the red curve is the nominal safety factor (right y axis) profile with one of its rational surface (red vertical line) around the pedestal. The green curve is the safety factor with 2% downshift, and the same rational surface is the green vertical line.

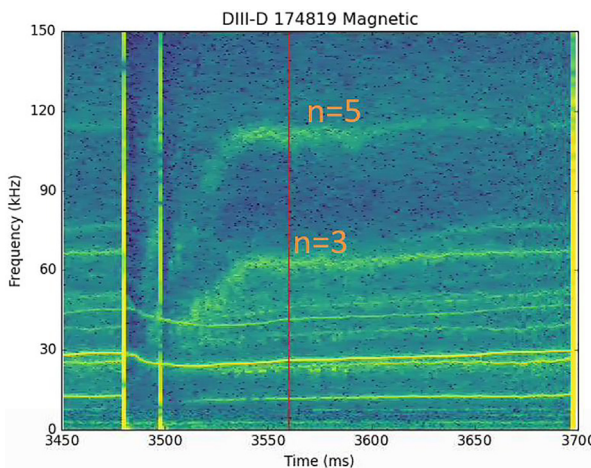


FIG. 17. Magnetic spectrogram for DIII-D discharge 174819 where the red line marked the time step the equilibrium is fitted, and the lower frequency band has toroidal mode number of $n = 3$ with frequency of 63 kHz, while the higher band has $n = 5$ with the frequency of 110 kHz.

It is worth noting that the stability of the model depends on the width of the horizontal lines. Similar to Fig. 16, if the stability boundary were more narrow, as left plot of Fig. 20, there will be fewer rational surfaces that the q profile will go through. On the other hand, right plot of Fig. 20 shows that a wide radial stability boundary will cause more rational surfaces to host unstable MTM. Therefore, it is crucial to know the radial range of stability boundary.

Taking the q profile with 2% downshift, a global linear simulation gyrokinetic scan of n_{tor} from 1 to 7 is performed. In Fig. 21, simulations show the mode numbers 3, 5, 6 are unstable, while $n = 4$ is stable, consistent with the prediction of the SLIM model.

The frequency (red horizontal lines) predicted by the global linear simulations provides a reasonable match to the experimental observation in Fig. 22 with a frequency of 70, 113, and 131 kHz.

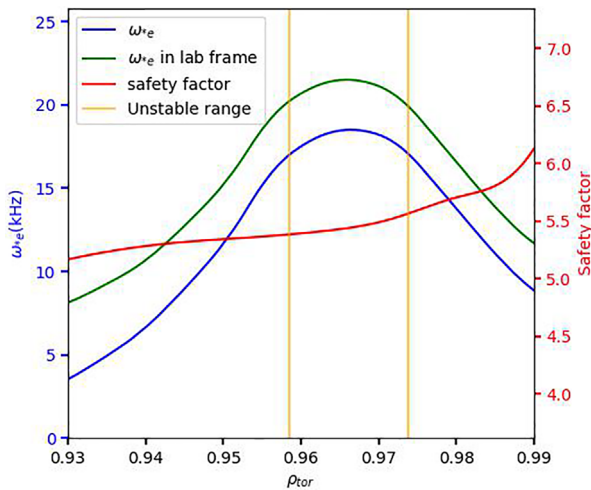


FIG. 18. The $\omega_{ce}(n = 1)$ in the plasma frame (blue) and the lab frame (green), safety factor (red). The radial range where MTM likely to be unstable (orange).

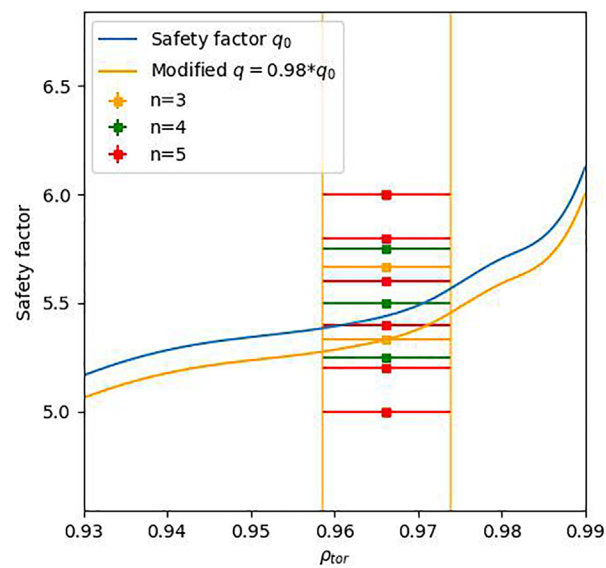


FIG. 19. Plots show the nominal safety factor profile (blue). The orange curve is the safety factor profile downshifted by 2%. The horizontal lines are the rational surfaces with toroidal mode numbers 3 (orange), 4 (green), and 5 (red). The width between the orange vertical lines is constrained by the radial stability boundary.

It is natural to ask why $n = 6$ is unstable from the gyrokinetic simulations while the experiment does not have such a magnetic frequency band. We find that even this very distinctive feature of the spectrogram can be interpreted using the SLIM mode. The question can be easily addressed by modifying the q profile in a different manner. Figure 23 shows the q profile has been up-shifted by 3%. The newly modified q profile can go through $n = 5$ at the center of the horizontal line which means the $n = 5$ has a rational surface located at the ω_{ce} peak, while the q profile goes through $n = 3$ at the edge in the left plot, which makes $n = 3$ unstable. We have observed that the radial stability boundary becomes more narrow with high toroidal mode numbers. In this case, it is likely the ratio ν/ω_{ce} is farther from the peak instability range for $n = 6$ than $n = 3$. Therefore, the $n = 6$ will be stable with 103% of the nominal q profile shown in the right plot.

Taking the 103% of the nominal q profile to do the global linear gyrokinetic simulations, simulation results shown in Fig. 24, we found that the $n = 3, 5$ are unstable (red dot), while $n = 4, 6$ are stable, which is now in precise agreement with the fluctuation data. This has been predicted by the SLIM using the idea of the rational surface alignment shown in Fig. 23.

The frequency (red horizontal lines) predicted by the global linear simulations using 103% of the nominal q profile provides a better match to the experimental observation in Fig. 25 with a frequency of 72 and 109 kHz.

There can be a systematic workflow to study and modify the profile as shown in Fig. 26. One can tell the toroidal mode numbers from the experiment.²⁹ From the nominal profile, one can plot out the rational surfaces similar to Fig. 16. Modifications of the q profile can be determined by changing the q profile so that it goes through the rational surfaces of desired mode numbers while avoiding the rest (illustrated in Fig. 23) based on the observation of toroidal mode numbers

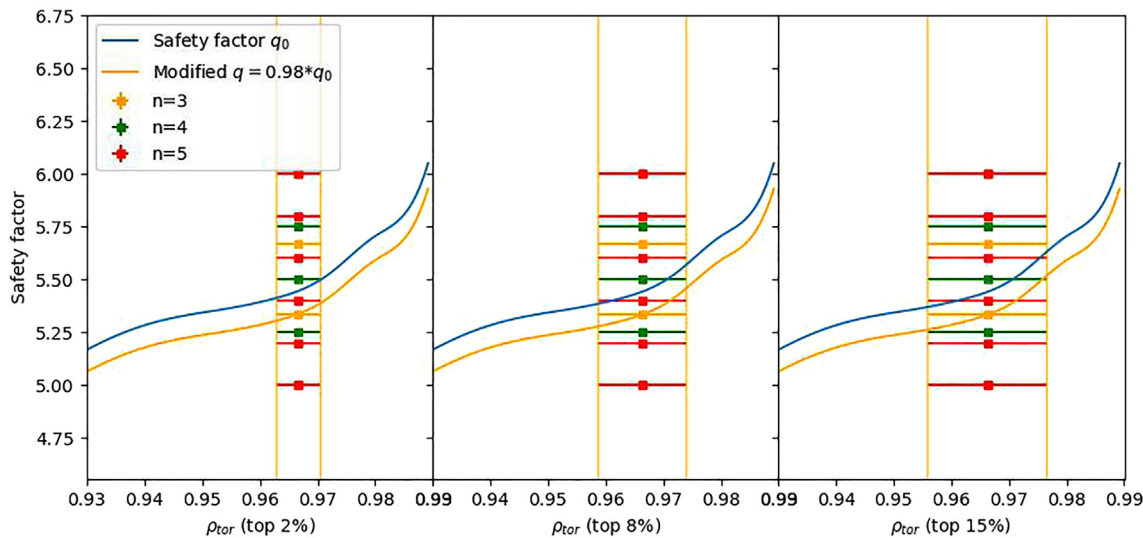


FIG. 20. Plot similar to Fig. 16 with left plot showing the rational surface with top 2% of ω_{*e} peak, middle plot shows top 8%, and the right plot shows top 15%.

from experimental data. After changing the q profile, one can use the SLIM model or simulations to find if the desired MTM is stable. One can also increase in the electron temperature gradient thus increases the drive to MTM instabilities. Such a procedure could be repeated until one gets the desired equilibrium. Using such a workflow to find the equilibrium provides a very systematic way to conduct sensitivity tests and provides a stringent constraint that may improve accuracy.

1. Characterizing offset stabilization

In order to characterize the rate of offset stabilization, we compare the GENE and SLIM calculations of the radial offset required to

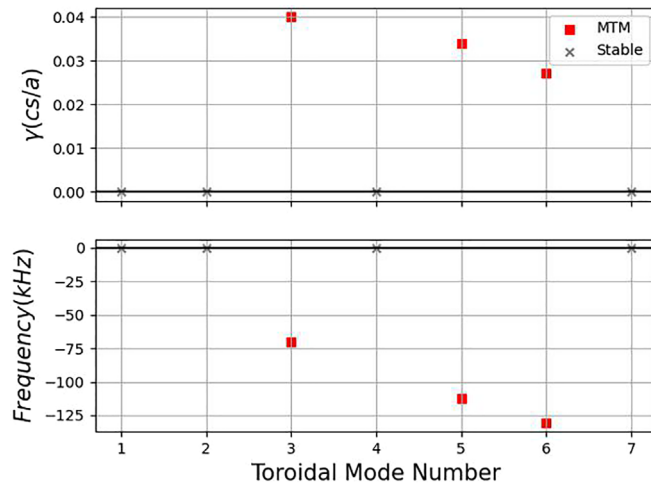


FIG. 21. Growth rate (top plot) and frequency in the lab frame (bottom plot) of the global linear simulations with toroidal mode number ranging from 1 to 7 with 98% of the nominal q profile. The red squares are the MTM, and the gray cross is the stable mode.

stabilize MTMs. We work from DIII-D discharge 174819 described immediately above.

Figure 27 shows a set of global linear simulations with the scaling of the q profile from -5% to $+5\%$ with 1% increment for toroidal mode number 3. Changing the safety factor will change the radial location of the rational surfaces. Only the rational surfaces that align closely with the peak of ω_{*e} (blue curve) become unstable (red vertical lines). For the ones that have unstable MTM, the $A_{||}$ amplitude is concentrated around the unstable rational surfaces shown in the bottom contour plot.

The rational surface alignment is a global effect that cannot be captured from local theory. Figure 28 shows the growth rate and frequency comparison between the global linear simulations (left column) and local linear simulations at the peak of ω_{*e} (right column)

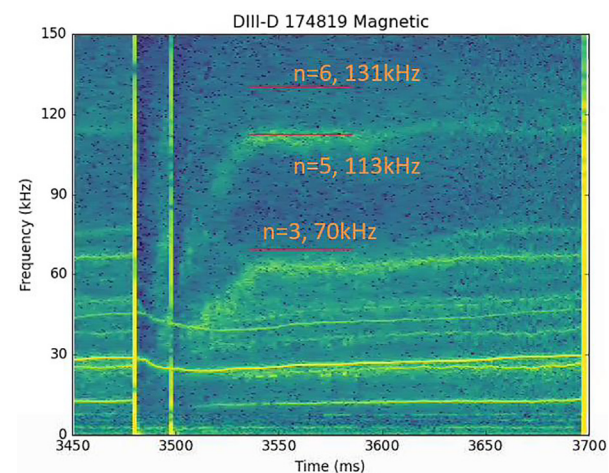


FIG. 22. The plot shows the experimental magnetic fluctuation frequency vs time. Overlaid are the red horizontal lines with frequencies predicted from the global linear simulations with $n = 3, 5, 6$.

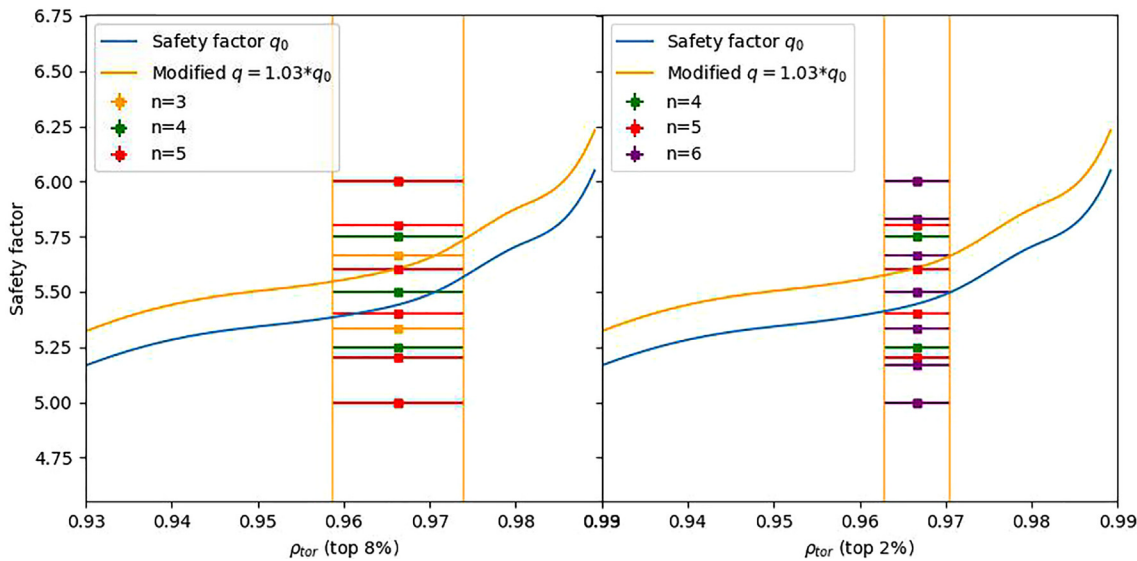


FIG. 23. The left plot shows the nominal safety factor profile (blue). The orange curve is the safety factor profile up-shifted by 3%. The horizontal lines are the rational surfaces with toroidal mode numbers 3 (orange), 4 (green), and 5 (red). The length of the horizontal lines is constrained by the radial stability boundary with top 8% of ω_{*e} . The right plot shows the rational surfaces with toroidal mode numbers 4 (green), 5 (red), and 6 (purple). The length of the horizontal lines is constrained by the radial stability boundary with top 3% of ω_{*e} .

with 95% to 105% of the nominal q profile. The global linear simulations show that MTM's stability is highly sensitive to the scaling to the q profile while local linear simulations show virtually no response with this 10% variation of q .

Both the SLIM model and global linear simulations demonstrate the stability of MTM is highly dependent on the offset $\frac{\mu}{x_*}$ as shown in Fig. 29. The value of μ is determined over the q scaling scan shown in Fig. 27 with 102%, 102.5%, 103%, 103.5%, and 104% of the nominal q profile. The SLIM model uses the same profile with a different μ as the

input parameter. Both SLIM and GENE have a similar sharp drop of growth rate as the rational surface goes further away from the ω_{*e} peak. To convert this parameter to the top percentage of the ω_{*e} for the radial stability boundary, it can be translated to top 8%. For the detail of the conversion, one can check the Appendix at the end of this article.

A similar q scaling scan with toroidal mode number 6 is also conducted, which is shown in Fig. 30. The $n=6$ has a narrower stability boundary, with $\mu/x_* \sim 0.15$, which represents top 2% of the ω_{*e} . The right plot in Fig. 23 shows the rational surfaces for $n=4, 5$, and 6 with

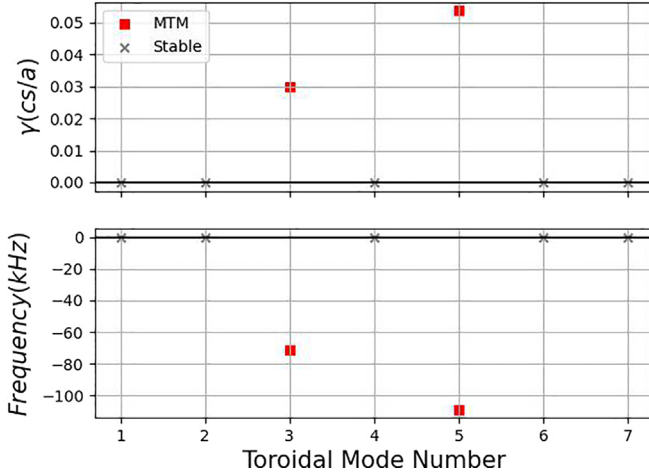


FIG. 24. Growth rate (top plot) and frequency in the lab frame (bottom plot) of the global linear simulations with toroidal mode number ranging from 1 to 7 with 103% of the nominal q profile. The red square is the MTM, and the gray cross is the stable modes.

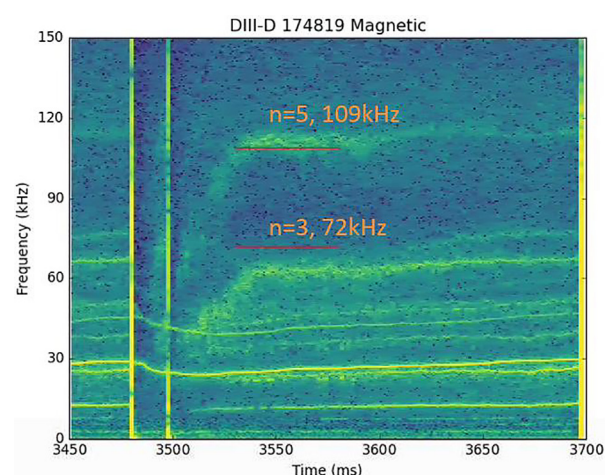


FIG. 25. The plot shows the experimental magnetic fluctuation frequency vs time. Overlaid are the red horizontal lines with frequencies predicted from the global linear simulations with $n=3, 5$.

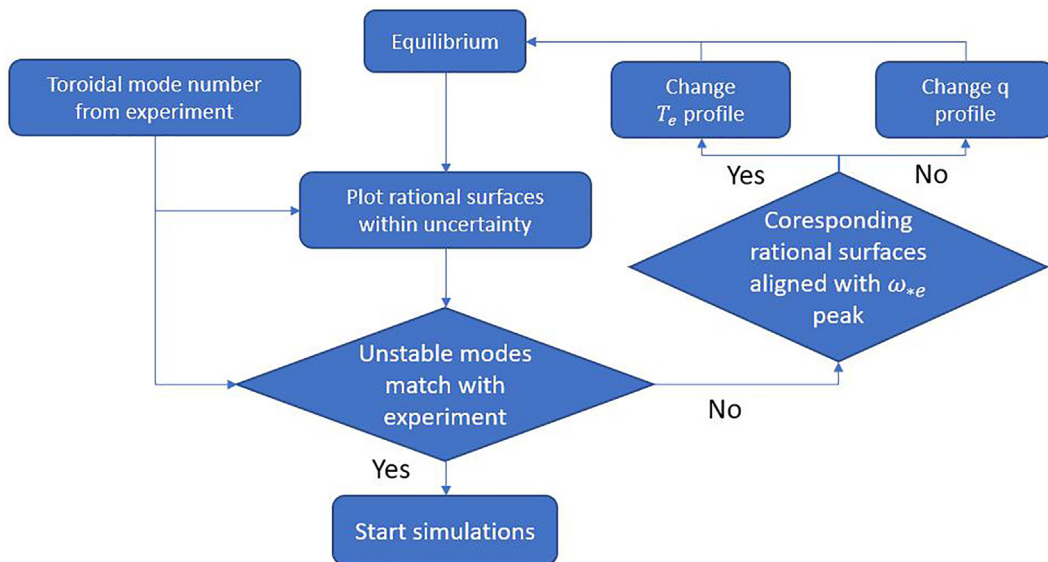


FIG. 26. The flow chart for equilibrium fitting using the SLIM model: one can calculate the toroidal mode number from MODESPEC, and then frequency and growth rate can be calculated from nominal equilibrium; if unstable MTM frequencies match with experimental observations, then the profile is good for further usage (such gyrokinetic simulations). Otherwise, one can modify the profile based on the desired rational surfaces which are present until the unstable MTM frequencies matches with the experimental observation.

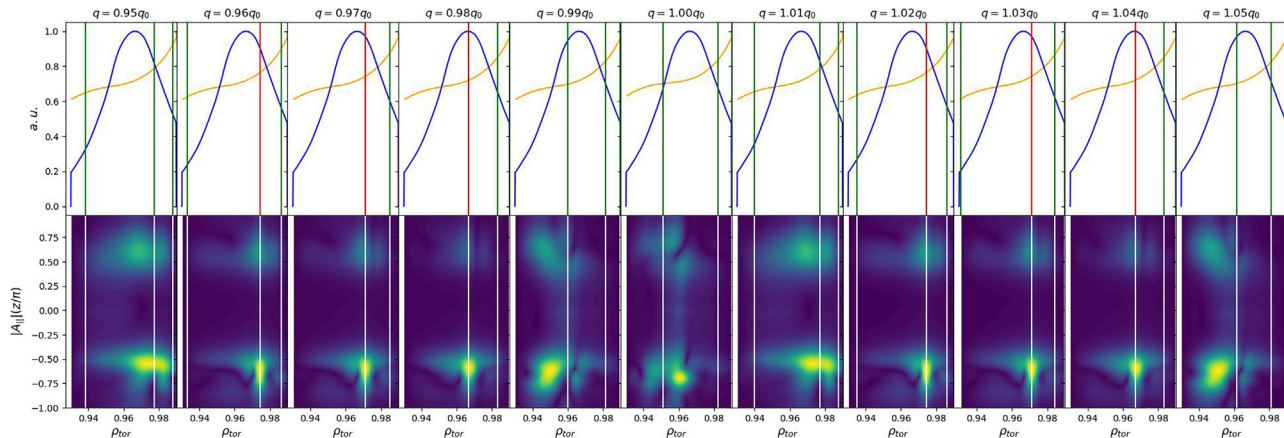


FIG. 27. The plot shows global linear simulations scaling of the q profile from -5% to $+5\%$ with 1% increment (from left to right). The top row shows the alignment of the rational surfaces with the peak of ω_{*e} , the blue curves are the ω_{*e} for $n = 3$, the orange curve is the q profile, the red vertical lines are the rational surfaces that host the unstable MTM, while the green vertical linear lines are stable. The bottom row shows the amplitude of $A_{||}$ (vector potential component that is parallel to B_0), the “brighter” in the contour plot, the higher $|A_{||}|$.

radial stability boundary of 2% of ω_{*e} peak. The 103% of the nominal q profile does not go through the rational surface with $n = 6$ and, therefore, makes $n = 6$ stable. This $n = 6$ scaling scan further justifies the choice of using 103% of the nominal q profile in order to match with the magnetic spectrogram.

IV. CONCLUSION AND FUTURE WORK

This paper introduces the slab-like MTM (SLIM) model for predicting and interpreting pedestal magnetic fluctuations. The model is motivated by the recent discovery that (1) MTMs are responsible for a

prominent class of edge magnetic fluctuations and (2) the alignment of the rational surfaces with the peak in the electron diamagnetic frequency governs the stability of these modes resulting in sensitive selection of unstable toroidal mode numbers. We define a criterion for the critical toroidal mode number below which this sensitive n -number selection can occur: $n_{crit} = \frac{\rho_{tor}}{2s\mu_{crit}}$, μ_{crit} is the radial stability boundary where MTM will become stable outside of it (μ is defined at Fig. 4).

The SLIM model encompasses two modes of operation: (1) a reduced model for global slab MTM, which has been shown to qualitatively reproduce global GENE results by identifying the stabilization of

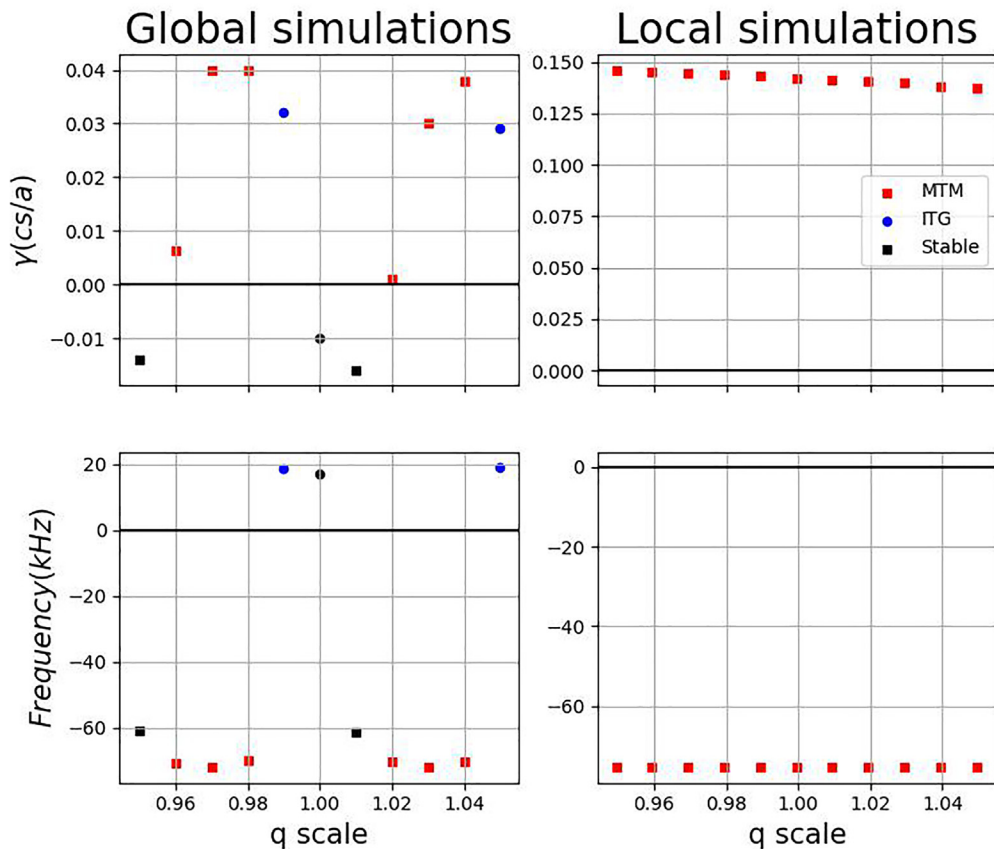


FIG. 28. Comparison between global linear simulations (left) and local linear simulations (right) with q scaling. The top row shows growth rate with different q scaling, and the bottom row shows frequency in the lab frame. The square is the MTM, circle is ion temperature gradient mode (ITG), colored is unstable, and black is stable.

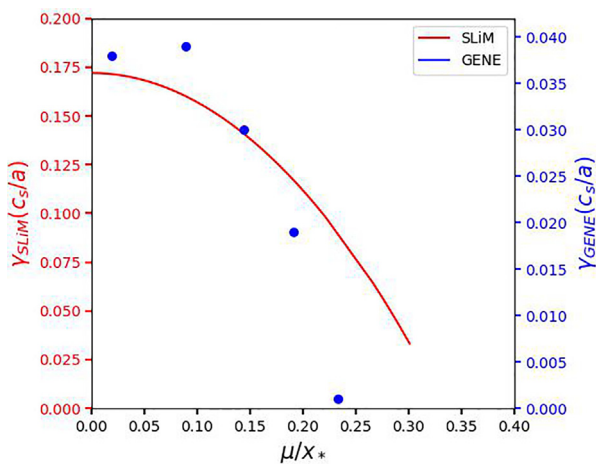


FIG. 29. The plot of MTM stability (growth rate) dependence on $\frac{\mu}{x_*}$ calculated from GENE global linear simulations (blue dots), and SLIM model (red curve). Left y axis is for the growth rate calculated from SLIM model, while the right y axis is for the growth rate computed from global linear GENE simulations.

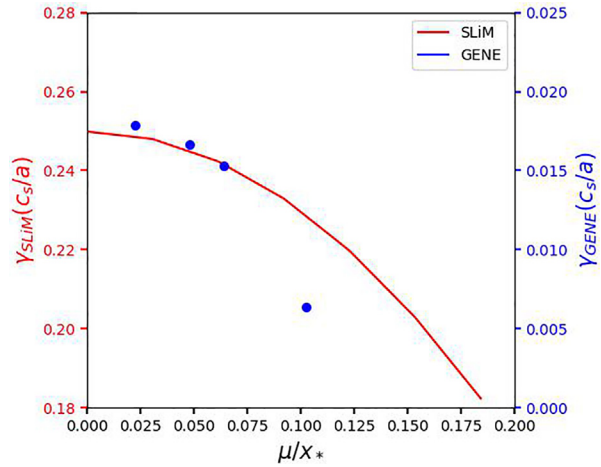


FIG. 30. The plot of MTM stability (growth rate) dependence on $\frac{\mu}{x_*}$ calculated from GENE global linear simulations (blue dots), and SLIM model (red curve). Left y axis is for the growth rate calculated from SLIM model, and right y axis is for the growth rate computed from global linear GENE simulations.

toroidal mode numbers, and (2) a heuristic approach for rapidly identifying stable toroidal mode numbers based on the location of their rational surfaces (the offset stabilization illustrated in Fig. 5). In combination with sparse application of global gyrokinetic simulations and local gyrokinetic simulations for curvature-driven MTM, this provides a rigorous yet efficient approach for predicting and interpreting edge magnetic fluctuations.

The major applications as SLiM so far are

- Matching the frequency with an experiment using SLiM and complemented with local linear simulations for high mode number MTM.
- Determining the poloidal mode numbers of unstable MTM's.
- Adapting the equilibrium by constraining the safety factor on the pedestal.

We have surveyed four discharges for which the concept of offset stabilization was successfully applied to magnetic spectrograms. The growing number of such analyses demonstrates the explanatory power of the concept of offset stabilization. Three of these studies have been described in previous publications. We review these and, in some cases, extend the analysis. We also present a new analysis of DIII-D discharge 174819. For this discharge, there are two frequency bands which can be experimentally identified as $n=3, 5$. Using the SLiM model to guide minor modifications to the q profile, we can precisely reproduce these mode numbers and frequencies with global linear gyrokinetic simulations. Perhaps, surprisingly, we can even construct a scenario wherein the $n=3$ mode is unstable while $n=6$ is stable (despite the fact that they share the same rational surface).

Additionally, we characterize the rate of stabilization with offset distance (distance between a rational surface and the peak). Moreover, we demonstrate that this is an intrinsically global effect that cannot be captured by a local flux tube approach.

The SLiM model performs well across different Tokamak devices. The rational surfaces located at the peak of $\omega_{*,e}$ with an integer multiple of its mode numbers explained the discrete band of the spectrogram. Under such an approach, simulations' high sensitivity of the magnetic profile has been explained. The SLiM model will provide information on the potential instability that was observed experimentally. By utilizing SLiM, one can obtain more information regarding the safety factor in the pedestal region which provides a route to very precise equilibrium reconstructions of the pedestal.

Future work (ongoing) will entail a more extensive survey of magnetic fluctuations on DIII-D using the SLiM model.

ACKNOWLEDGMENTS

This material is based upon work supported by the U.S. Department of Energy, Office of Science, Office of Fusion Energy Sciences, using the DIII-D National Fusion Facility, a DOE Office of Science user facility, under Award Nos. DE-FC02-04ER54698, DE-AC02-05CH11231, DE-AC02-09CH11466, DE-FG02-04ER54761, and DE-SC0019004.

This work was supported by U.S. DOE Contract No. DE-FG02-04ER54742 at the Institute for Fusion Studies (IFS) at the University of Texas at Austin.

This research used resources of the National Energy Research Scientific Computing Center, a DOE Office of Science User Facility.

We acknowledge the CINECA award under the ISCRA initiative, for the availability of high-performance computing resources and support.

This research was supported at Oak Ridge National Laboratory supported by the Office of Science of the U.S. Department of Energy under Contract No. DE-AC05-00OR22725.

This work has been carried out within the framework of the EUROfusion Consortium and has received funding from the Euratom research and training programme 2014–2018 and 2019–2020 under Grant Agreement No. 633053. The views and opinions expressed herein do not necessarily reflect those of the European Commission.

This scientific paper has been published as part of the international project co-financed by the Polish Ministry of Science and Higher Education within the program called “PMW” for year.

This report was prepared as an account of work sponsored by an agency of the U.S. Government. Neither the U.S. Government nor any agency thereof, nor any of their employees, makes any warranty, express or implied, or assumes any legal liability or responsibility for the accuracy, completeness, or usefulness of any information, apparatus, product, or process disclosed, or represents that its use would not infringe privately owned rights. Reference herein to any specific commercial product, process, or service by trade name, trademark, manufacturer, or otherwise does not necessarily constitute or imply its endorsement, recommendation, or favoring by the U.S. Government or any agency thereof. The views and opinions of authors expressed herein do not necessarily state or reflect those of the U.S. Government or any agency thereof.

This manuscript has been authored by UT-Battelle, LLC, under Contract No. DE-AC05-00OR22725 with the U.S. Department of Energy (DOE). The publisher acknowledges the U.S. government license to provide public access under the DOE Public Access Plan (<http://energy.gov/downloads/doe-public-access-plan>).

AUTHOR DECLARATIONS

Conflict of Interest

The authors have no conflicts to disclose.

DATA AVAILABILITY

The data that support the findings of this study are openly available in SLiM, at <https://github.com/maxtcurie/SLiM>, Ref. 32.

APPENDIX: ADDITIONAL INFORMATION ON THEORY AND SIMULATIONS

1. A brief discussion of $\sigma_{||}(\omega, x)$

A detailed calculation and discussion of $\sigma_{||}(\omega, x)$ can be found in Larakers *et al.* (2020).²⁴ The conductivity is computed from the $v_{||}$ moment of the perturbed guiding center distribution function. It contains the essential spatial dependence of the diamagnetic frequencies which causes offset stabilization. Equation (A1) shows the form of the final result

$$\sigma_{||} = \frac{-\omega_{pe}^2}{2\pi\nu\omega} [(\omega - \omega_{*n} - \omega_{*T})L_{11} - \omega_{*T}L_{12}], \quad (\text{A1})$$

where $\omega_{pe} = \frac{4\pi n e^2}{m_e}$ and $\omega_{*n} = \frac{k_y \rho_s c_s}{L_{n_e}}$ and $\omega_{*T} = \frac{k_y \rho_s c_s}{L_{T_e}}$. Here, L_{11} and L_{12} are “transport coefficients” that represent the parametric response of the electrons for arbitrary frequency, collisionality, and

k_{\parallel} . Due to magnetic shear, k_{\parallel} has spatial dependence, and thus, the transport coefficients have a spatial structure with characteristic length scale $x_{\sigma} = \omega/k'_{\parallel}v_e$. Due to the fact that electrons become adiabatic at large k_{\parallel} , these functions decay to zero for large k_{\parallel} .

Larakers *et al.* (2020)²⁴ computes a variety of forms for these transport coefficients. We have applied the rational form computed using the full collision operator and including Z_{eff} , the full definition is found in Appendix B of Larakers *et al.* (2020).²⁴ This description of the conductivity provides electron response across the full frequency range and spatial range.

The basic form of conductivity describes the essential physics of the MTM. The coefficient $\omega_{pe}^2/2\pi\nu$ is numerically large in the pedestal, and for the electromagnetic equations to be balanced, the zeroth-order dispersion relation becomes $\sigma=0$. This indicates that mode will have a real frequency $\omega \approx \omega_{*n} + \omega_{*T}$, and the growth rate will be set by a phase difference in the L_{11} and L_{12} response. This phase difference is equivalent to the time-dependent thermal force described in Hassam (1980).³¹

The spatial dependence of the diamagnetic frequencies is seen to be important when the characteristic length scale of variation is of order to the spatial width of the localized transport coefficients. Let x_* be the length scale of variation of the diamagnetic frequencies and, $x_{\sigma} = \frac{\omega R}{k_{\perp}v_e}$. For $r = x_*/x_{\sigma} \ll 1$, the local value of ω_{*n} and ω_{*T} is all that is important. For $r \sim 1$, the spatial structure of the ω_{*n} and ω_{*T} can affect the mode we expect strong offset stabilization.

2. Definitions of variable

It is important to show the conversion of μ/x_* describes the spread of ω_{*e} by fitting the ω_{*e} with Gaussian function, $\omega_{*e} = \omega_0 \cdot e^{-x^2/x_*^2}$. In other word, $x_* = \sqrt{2}\sigma$ where σ is the standard deviation of Gaussian distribution. At $x = \mu$, $\omega_{*e} = \omega_0 \cdot e^{-\mu^2/x_*^2}$, it can be converted to top $(1 - e^{-(\mu/x_*)^2}) \cdot 100\%$ of the ω_{*e} . However, such calculation is just an estimation since the ω_{*e} is not a perfect Gaussian distribution function.

3. Details on simulations

One can check the details of the simulations on the paper of the DIII-D discharge 162940 by Hassan,⁷ and JET discharge 78697 by Hatch.⁶

For DIII-D discharge 174819, Table II shows the parameters used for local linear and global linear simulations. A convergence test has been performed by conducting simulations with twice the resolution and getting the same numerical result.

TABLE II. Important parameters used in the local linear and global linear simulations.

Simulation type	nx	nz	nv	nw	Hypz	$E \times B$ shear (on/off)
Local linear	9	96	48	16	-2	Off
Global linear	256	96	32	12	-2	On

REFERENCES

- ¹F. Wagner, G. Becker, K. Behringer, D. Campbell, A. Eberhagen, W. Engelhardt, G. Fussmann, O. Gehre, J. Gernhardt, V. Gierke, G. Haas, M. Huang, F. Karger, M. Keilhacker, O. Klüber, M. Kornherr, K. Lackner, G. Lisitano, G. G. Lister, H. M. Mayer, D. Meisel, E. R. Müller, H. Murmann, H. Niedermeyer, W. Poschenrieder, H. Rapp, H. Röhr, F. Schneider, G. Siller, E. Speth, A. Stäbler, K. H. Steuer, G. Venus, O. Vollmer, and Z. Yü, "Regime of improved confinement and high beta in neutral-beam-heated divertor discharges of the ASDEX tokamak," *Phys. Rev. Lett.* **49**, 1408–1412 (1982).
- ²K. H. Burrell, "Effects of $E \times B$ velocity shear and magnetic shear on turbulence and transport in magnetic confinement devices," *Phys. Plasmas* **4**, 1499–1518 (1997).
- ³M. Kotschenreuther, X. Liu, D. Hatch, S. Mahajan, L. Zheng, A. Diallo, R. Groebner, DIII-D Team, J. Hillesheim, C. Maggi, C. Giroud, F. Koechl, V. Parail, S. Saarelma, E. Solano, A. Chankin, and JET Contributors, "Gyrokinetic analysis and simulation of pedestals to identify the culprits for energy losses using 'fingerprints,'" *Nucl. Fusion* **59**, 096001 (2019).
- ⁴J. Chen, D. L. Brower, W. X. Ding, Z. Yan, T. Osborne, E. Strait, M. Curie, D. R. Hatch, M. Kotschenreuther, X. Jian, M. R. Halfmoon, and S. M. Mahajan, "Internal measurement of magnetic turbulence in ELMMy H-mode tokamak plasmas," *Phys. Plasmas* **27**, 120701 (2020).
- ⁵D. Hatch, M. Kotschenreuther, S. Mahajan, P. Valanju, F. Jenko, D. Told, T. Görler, and S. Saarelma, "Microtearing turbulence limiting the JET-ILW pedestal," *Nucl. Fusion* **56**, 104003 (2016).
- ⁶D. Hatch, M. Kotschenreuther, S. Mahajan, M. Pueschel, C. Michoski, G. Merlo, E. Hassan, A. Field, L. Frassinetti, C. Giroud, J. Hillesheim, C. Maggi, C. P. von Thun, C. Roach, S. Saarelma, D. Jarema, F. Jenko, and JET Contributors, "Microtearing modes as the source of magnetic fluctuations in the JET pedestal," *Nucl. Fusion* **61**, 036015 (2021).
- ⁷E. Hassan, D. Hatch, M. Halfmoon, M. Curie, M. Kotchenreuther, S. Mahajan, G. Merlo, R. Groebner, A. Nelson, and A. Diallo, "Identifying the microtearing modes in the pedestal of DIII-D H-modes using gyrokinetic simulations," *Nucl. Fusion* **62**, 026008 (2021).
- ⁸A. O. Nelson, F. M. Laggner, A. Diallo, D. Smith, A. Xing, R. Shousha, and E. Kolemen, "Time-dependent experimental identification of inter-ELM microtearing modes in the tokamak edge on DIII-D," *Nucl. Fusion* **61**, 116038 (2021).
- ⁹M. Halfmoon, D. Hatch, M. Kotschenreuther, S. Mahajan, A. Nelson, E. Kolemen, M. Curie, A. Diallo, R. Groebner, and E. Hassan, "Gyrokinetic analysis of inter-ELM transport mechanisms in a DIII-D pedestal," *Phys. Plasmas* (unpublished).
- ¹⁰A. Diallo, J. Dominski, K. Barada, M. Knolker, G. J. Kramer, and G. McKee, "Direct observation of nonlinear coupling between pedestal modes leading to the onset of edge localized modes," *Phys. Rev. Lett.* **121**, 235001 (2018).
- ¹¹J. Dominski and A. Diallo, "Transition of a network of nonlinear interactions into a regime of strong nonlinear fluctuations: A paradigm for the edge localized mode onset," *Phys. Plasmas* **28**, 092306 (2021).
- ¹²J. Dominski and A. Diallo, "Identification of a network of nonlinear interactions as a mechanism triggering the onset of edge localized modes," *Plasma Phys. Controlled Fusion* **62**, 095011 (2020).
- ¹³C. P. Perez, H. R. Koslowski, T. C. Hender, P. Smeulders, A. Loarte, P. J. Lomas, G. Saibene, R. Sartori, M. Becoulet, T. Eich, R. J. Hastie, G. T. A. Huysmans, S. Jachmich, A. Rogister, F. C. Schüller, and JET EFDA Contributors, "Washboard modes as ELM-related events in JET," *Plasma Phys. Controlled Fusion* **46**, 61–87 (2003).
- ¹⁴A. Diallo, J. W. Hughes, M. Greenwald, B. LaBombard, E. Davis, S.-G. Baek, C. Theiler, P. Snyder, J. Canik, J. Walk, T. Golfinopoulos, J. Terry, M. Churchill, A. Hubbard, M. Porkolab, L. Delgado-Aparicio, M. L. Reinke, A. White, and Alcator C-Mod Team, "Observation of edge instability limiting the pedestal growth in tokamak plasmas," *Phys. Rev. Lett.* **112**, 115001 (2014).
- ¹⁵A. Diallo, R. J. Groebner, T. L. Rhodes, D. J. Battaglia, D. R. Smith, T. H. Osborne, J. M. Canik, W. Guttenfelder, and P. B. Snyder, "Correlations between quasi-coherent fluctuations and the pedestal evolution during the inter-edge localized modes phase on DIII-D," *Phys. Plasmas* **22**, 056111 (2015).
- ¹⁶F. M. Laggner, E. Wolfrum, M. Cavedon, F. Mink, E. Viezzer, M. G. Dunne, P. Manz, H. Doerk, G. Birkenmeier, R. Fischer, S. Fietz, M. Maraschek, M.

- Willensdorfer, and F. Aumayr, "High frequency magnetic fluctuations correlated with the inter-ELM pedestal evolution in ASDEX upgrade," *Plasma Phys. Controlled Fusion* **58**, 065005 (2016).
- ¹⁷F. Laggner, A. Diallo, M. Cavedon, and E. Kolemen, "Inter-ELM pedestal localized fluctuations in tokamaks: Summary of multi-machine observations," *Nucl. Mater. Energy* **19**, 479–486 (2019).
- ¹⁸J. Chen, D. Brower, W. Ding, R. Yoneda, and D. Finkenthal, "Correlation polarimeter-interferometer in the DIII-D tokamak," *Rev. Sci. Instrum.* **92**, 043502 (2021).
- ¹⁹J. Chen, W. X. Ding, D. L. Brower, D. Finkenthal, C. Muscatello, D. Taussig, and R. Boivin, "Faraday-effect polarimeter diagnostic for internal magnetic field fluctuation measurements in DIII-D," *Rev. Sci. Instrum.* **87**, 11E108 (2016).
- ²⁰J. Chen, D. L. Brower, W. X. Ding, Z. Yan, M. Curie, M. Kotschenreuther, T. Osborne, E. Strait, D. R. Hatch, M. R. Halfmoon, S. M. Mahajan, and X. Jian, "Pedestal magnetic turbulence measurements in ELMy H-mode DIII-D plasmas by Faraday-effect polarimetry," *Phys. Plasmas* **28**, 022506 (2021).
- ²¹D. M. Hatch, M. Kotschenreuther, S. M. Mahajan, G. Merlo, A. R. Field, C. Giroud, J. C. Hillesheim, C. F. Maggi, C. P. von Thun, C. M. Roach, S. Saarelma, and JET Contributors, "Direct gyrokinetic comparison of pedestal transport in JET with carbon and ITER-like walls," *Nucl. Fusion* **59**, 086056 (2019).
- ²²D. R. Hatch, M. T. Kotschenreuther, S. M. Mahajan, M. Halfmoon, E. Hassan, G. Merlo, C. Michoski, J. Canik, A. Sontag, I. Joseph, M. Umansky, W. Guttenfelder, A. Diallo, R. Groebner, A. O. Nelson, F. Laggner, J. Hughes, and S. Mordijk, "Fy19 FES theory performance target (final report)," (2020); available at <https://www.osti.gov/servlets/purl/1615233/>.
- ²³J. L. Larakers, M. Curie, D. R. Hatch, R. D. Hazeltine, and S. M. Mahajan, "Global theory of microtearing modes in the tokamak pedestal," *Phys. Rev. Lett.* **126**, 225001 (2021).
- ²⁴J. L. Larakers, R. D. Hazeltine, and S. M. Mahajan, "A comprehensive conductivity model for drift and micro-tearing modes," *Phys. Plasmas* **27**, 062503 (2020).
- ²⁵F. Jenko, W. Dorland, M. Kotschenreuther, and B. N. Rogers, "Electron temperature gradient driven turbulence," *Phys. Plasmas* **7**, 1904–1910 (2000).
- ²⁶T. Görler, X. Lapillonne, S. Brunner, T. Dannert, F. Jenko, F. Merz, and D. Told, "The global version of the gyrokinetic turbulence code gene," *J. Comput. Phys.* **230**, 7053–7071 (2011).
- ²⁷J. F. Drake and Y. C. Lee, "Kinetic theory of tearing instabilities," *Phys. Fluids* **20**, 1341–1353 (1977).
- ²⁸N. T. Gladd, J. F. Drake, C. L. Chang, and C. S. Liu, "Electron temperature gradient driven microtearing mode," *Phys. Fluids* **23**, 1182–1192 (1980).
- ²⁹E. J. Strait, "Magnetic diagnostic system of the DIII-D tokamak," *Rev. Sci. Instrum.* **77**, 023502 (2006).
- ³⁰O. Meneghini, S. Smith, L. Lao, O. Izacard, Q. Ren, J. Park, J. Candy, Z. Wang, C. Luna, V. Izzo, B. Grierson, P. Snyder, C. Holland, J. Penna, G. Lu, P. Raum, A. McCubbin, D. Orlov, E. Belli, N. Ferraro, R. Prater, T. Osborne, A. Turnbull, and G. Staebler, "Integrated modeling applications for tokamak experiments with OMFIT," *Nucl. Fusion* **55**, 083008 (2015).
- ³¹A. B. Hassam, "Fluid theory of tearing instabilities," *Phys. Fluids* **23**, 2493–2497 (1980).
- ³²M. Curie (2022). "Slab-like microtearing (SLiM) model," GitHub repository. <https://github.com/maxcurie/SLiM>